PLANETARY SCIENCE

Hydrogen peroxide at the poles of Ganymede

Samantha K. Trumbo[1]*, Michael E. Brown[2], Dominique Bockelée-Morvan[3], Imke de Pater[4], Thierry Fouchet[3], Michael H. Wong[5], Stéphanie Cazaux[6,7], Leigh N. Fletcher[8], Katherine de Kleer[2], Emmanuel Lellouch[3], Alessandro Mura[9], Olivier Poch[10], Eric Quirico[10], Pablo Rodriguez-Ovalle[3], Mark R. Showalter[11], Matthew S. Tiscareno[11], Federico Tosi[9]

Ganymede is the only satellite in the solar system known to have an intrinsic magnetic field. Interactions between this field and the Jovian magnetosphere are expected to funnel most of the associated impinging charged particles, which radiolytically alter surface chemistry across the Jupiter system, to Ganymede's polar regions. Using observations obtained with JWST as part of the Early Release Science program exploring the Jupiter system, we report the discovery of hydrogen peroxide, a radiolysis product of water ice, specifically constrained to the high latitudes. This detection directly implies radiolytic modification of the polar caps by precipitation of Jovian charged particles along partially open field lines within Ganymede's magnetosphere. Stark contrasts between the spatial distribution of this polar hydrogen peroxide, those of Ganymede's other radiolytic oxidants, and that of hydrogen peroxide on neighboring Europa have important implications for understanding water-ice radiolysis throughout the solar system.

INTRODUCTION

The radiolysis of water ice is a ubiquitous process in the ice-rich outer solar system and is known to be an important contributor to the surface compositions of Jupiter's icy Galilean satellites, which are all subject to particle irradiation from the extended Jovian magnetosphere (*1*). The impinging energetic charged particles break apart surface water molecules and create ions and radicals, resulting in subsequent reactions and the formation of hydrogen and oxygen products (*2*). As a result, all three moons feature molecular oxygen (O_2) in their tenuous atmospheres (*3*–*6*) and trapped within their surfaces (*7*, *8*). The surface of Ganymede is also thought to contain the related radiolytic product ozone (O_3), based on a broad ultraviolet (UV) absorption consistent with the O_3 Hartley band (*9*, *10*). However, although Ganymede's magnetic field (*11*, *12*)—the only known intrinsic magnetic field of any planetary satellite—is expected to direct most of the irradiating particles to the high latitudes (*13*), Ganymede's radiolytically produced O_2 and O_3 exist primarily on the sheltered trailing hemisphere (*7*, *9*, *10*), with the O_2 clearly constrained to low latitudes (*14*, *15*), although the O_3 may vary with solar zenith angle resulting in relative enhancements at the trailing poles and morning and evening limbs (*10*, *16*). Ganymede's polar caps (*17*, *18*) have been suggested to reflect bright frosts formed via the re-deposition of H_2O sputtered as a result of the predicted high-latitude bombardment (*18*, *19*), but no direct evidence for the anticipated enhanced chemical alteration of the poles by radiolysis has been seen to date.

It is also curious that the minor water radiolysis product hydrogen peroxide (H_2O_2) has not been identified anywhere on Ganymede. H_2O_2 has been clearly detected via a strong 3.5 μm absorption on the surface of Europa (*20*, *21*), despite Europa exhibiting ~10 times weaker O_2 signatures than Ganymede's (*8*) and no detected O_3 band (*22*). Although Ganymede's UV spectrum was suggested as possibly consistent with the inclusion of small amounts of H_2O_2 at equatorial leading latitudes (*23*), and one of the many unconfirmed possible absorptions in orbit-averaged infrared spectra from *Juno*'s JIRAM instrument was noted to fall near the 3.5 μm band of H_2O_2 in the most poleward-looking orbits (*24*), the distinctive H_2O_2 feature identified on Europa has not been clearly seen. Its apparent absence, the puzzling distributions of Ganymede's radiolytic O_2 and O_3, and the overall differences in assemblages of radiolytic oxidants on Europa and Ganymede have posed challenges for our understanding of how water radiolysis proceeds on icy bodies. Here, we use observations of Ganymede's surface obtained with James Webb Space Telescope (JWST) as part of the Early Release Science (ERS) program exploring the Jupiter system to clearly identify the 3.5 μm band of H_2O_2 for the first time and demonstrate that it is constrained to Ganymede's polar caps.

RESULTS

JWST observed Ganymede with the NIRSpec Integral Field Unit (IFU) across two visits in August 2022 (Table 1), providing spectral image cubes across the 2.9 to 5.2 μm range at a resolving power of ~2700. The cubes have a spatial pixel size of 0.1 arc sec × 0.1 arc sec (corresponding to ~310 km × 310 km at the sub-observer point). Some of these spatial pixels within the JWST NIRSpec IFU cubes of Ganymede show a subtle, yet distinct absorption feature near 3.5 μm with a minimum between 3.495 and 3.515 μm (Fig. 1), which resembles the established H_2O_2 signature on Europa (*20*, *21*). To facilitate comparison to Europa's H_2O_2 band, we take the

[1]Cornell Center for Astrophysics and Planetary Science, Cornell University, Ithaca, NY 14853, USA. [2]Division of Geological and Planetary Sciences, California Institute of Technology, Pasadena, CA 91125, USA. [3]LESIA, Observatoire de Paris, Université PSL, Sorbonne Université, Université Paris Cité, CNRS, Meudon 92195, France. [4]Departments of Astronomy and of Earth and Planetary Science, University of California, Berkeley, CA 94720, USA. [5]Center for Integrative Planetary Science, University of California, Berkeley, CA 94720-3411, USA. [6]Faculty of Aerospace Engineering, Delft University of Technology, Delft, Netherlands. [7]Leiden Observatory, Leiden University, P.O. Box 9513, NL 2300 RA, Leiden, Netherlands. [8]School of Physics and Astronomy, University of Leicester, Leicester LE1 7RH, UK. [9]Istituto Nazionale di AstroFisica–Istituto di Astrofisica e Planetologia Spaziali (INAF-IAPS), Rome, Italy. [10]Université Grenoble Alpes, Centre National de la Recherche Scientifique (CNRS), Institut de Planétologie et d'Astrophysique de Grenoble (IPAG), Grenoble 38000, France. [11]SETI Institute, Mountain View, CA 94043, USA.
*Corresponding author. Email: skt39@cornell.edu

Table 1. JWST NIRSpec IFU observations of Ganymede.

Date (UT)	Time (UT)	Central longitude	Central latitude	Angular diameter	Filter	Grating	Exposure time (s)	Dithers
3 August 2022	19:32	269°W	2.54°S	1.67 arc sec	F290LP	G395H	429.5	4
7 August 2022	01:10	72°W	2.55°S	1.69 arc sec	F290LP	G395H	429.5	4

high signal-to-noise ground-based leading-hemisphere spectrum of Europa from (*21*), which exhibits a strong 3.5 μm absorption, fit and remove a third-order polynomial continuum from 3.4 to 3.67 μm (excluding the range corresponding to the visible feature), and compare the shape of the residual absorption to Ganymede's 3.5 μm band, which we isolate using identical continuum parameters. In doing so, we scale the strength of Europa's absorption to best fit that of Ganymede's.

Figure 1B shows the result of this comparison for select latitudinal averages containing the strongest 3.5 μm signatures on Ganymede. We find that the two bands are nearly identical in shape, with Ganymede's also displaying the characteristic asymmetry and long-wavelength tail of H_2O_2 dispersed in water ice (*25*). On the basis of the quality of this spectral match, Ganymede's 3.5 μm band can be conclusively identified as resulting from H_2O_2. Figure 1 also illustrates the large-scale geographic trends in the distribution of Ganymede's H_2O_2, demonstrating its apparent preference for the high latitudes, particularly those of the leading hemisphere. For the purposes of comparison to Europa, we follow the method used to estimate its H_2O_2 abundance from the ground-based spectra (*21*) to approximate the H_2O_2 column density of the optically sensed layer and corresponding concentration of H_2O_2 relative to water at the upper latitudes of Ganymede's leading hemisphere. We find that the estimated values derived from the spectra in Fig. 1B vary from ~3×10^{16} molecules/cm^2 and ~0.02%, respectively, for the ±30° to 60° latitude bins to ~5×10^{16} molecules/cm^2 and ~0.035% for the highest latitude bins. We find values of ~7.8×10^{16} molecules/cm^2 and ~0.05% relative to water for the spectrum of Europa's leading hemisphere, which is approximately a factor of 2 lower than the value reported in (*21*) using a different polynomial fit, highlighting one of the caveats associated with such estimates.

To fully explore the distribution of the H_2O_2, we measure the strength of the 3.5 μm absorption within each spatial pixel of the two spectral image cubes (see Materials and Methods) to produce maps of Ganymede's H_2O_2 band (Fig. 2). Again, we find that the H_2O_2 is most clearly present only at the upper latitudes, and particularly at those of the leading hemisphere, which shows sharp boundaries at roughly ±30° to 35° latitude. In comparison, the trailing hemisphere shows only very weak H_2O_2 bands, which are faintly visible in spectra of the highest latitudes. The latitudinal boundaries in H_2O_2 on the leading hemisphere are roughly co-located with the edge of Ganymede's polar caps at ±40° (*17*, *18*) and with the onset of surface bombardment by most of the impinging Jovian magnetospheric particles (*13*, *18*), which are expected to be deflected away from the equator by Ganymede's intrinsic magnetic field. The boundary of the polar H_2O_2 seen in Fig. 2 corresponds quite well to the expected transition between open and closed field lines (*18*). This geography implies that the H_2O_2 is forming in polar ice via irradiation by particles that precipitate along partially open field lines to affect the polar regions. The polar caps have been suggested to reflect the re-deposition of resulting sputtered H_2O to form bright frosts (*18*, *19*), and the polar regions show evidence for finer-grained ice than does the rest of the surface (*26*, *27*). In addition, they stand out as the most ice-rich locations in spectroscopic maps of ice distribution (*28*, *29*).

As the best available proxy for water ice in the JWST cubes, we measure the strength of the double ~3.1 μm Fresnel H_2O reflectance peak, which is visible to varying degrees in the spectra of Fig. 1, although it is characteristically stronger and more structured in crystalline ice than in amorphous ice and can change with temperature (*30*–*32*). The resulting distributions are also shown in Fig. 2 and agree well with the geography deduced from shorter-wavelength infrared H_2O bands for the leading hemisphere (*28*, *29*), which show the leading-hemisphere poles to be the most ice-rich regions on the surface and also highlight the icy crater Tros (11°N, 27°W) that is pulled out in our map. In general agreement with past observations (*28*, *33*, *34*), the trailing hemisphere appears broadly less icy in our maps than does the leading, which is consistent with the trailing hemisphere having a higher abundance of dark non-ice material (*28*). However, the trailing-hemisphere geography of the Fresnel peak is curious, as it shows slight enhancements at the poles, but the strongest signatures on the morning limb. Understanding this phenomenon is beyond the scope of this paper, but it is possible that temperature effects on peak strength (*32*) or potential day/night sublimation/condensation effects with Ganymede's atmosphere (*35*) should be considered.

Overall, Ganymede's H_2O_2 clearly prefers ice-rich regions of the surface, which is unsurprising given that water is a necessary precursor for its formation. Water-ice abundance may account for the contrast in 3.5 μm band area between the icier upper latitudes of the leading hemisphere and less-icy upper latitudes of the trailing hemisphere. However, precursor ice availability likely cannot account for the latitudinal constraints of the strongest bands, which are restricted to higher latitudes than much of the ice-rich terrain, and which instead imply a need for enhanced irradiation, low temperatures, or both.

DISCUSSION

H_2O_2 is now the third water-ice radiolysis product detected on the surface of Ganymede and the first to indicate polar radiolysis driven by Jovian magnetospheric particles directed by Ganymede's own magnetic field. Somewhat counterintuitively, it appears essentially anticorrelated with the other two water-ice radiolysis products, O_2 and O_3, both of which are most prominent on the trailing hemisphere (*7*, *9*, *10*). Ganymede's surface O_2 signatures are strongest specifically at the low latitudes of the trailing hemisphere (*8*, *15*), in total contrast to the polar, leading-hemisphere H_2O_2 we detect here.

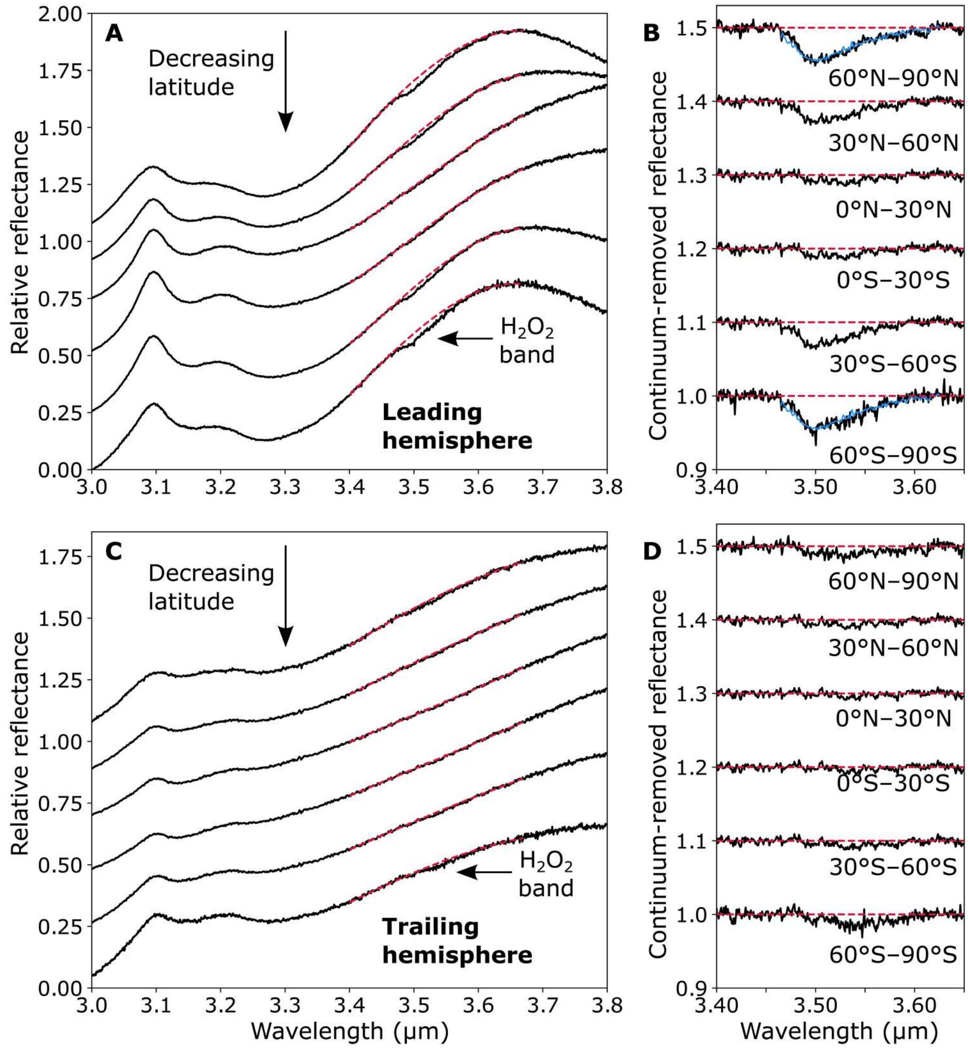

Fig. 1. Average JWST spectra of Ganymede for different latitude bins across the leading and trailing hemispheres. (**A**) Average spectra representing 30° latitude bins for the leading-hemisphere observation. The bins decrease in latitude from 60°N to 90°N for the top spectrum to 60°S to 90°S for the bottom spectrum. All of the spectra have been normalized at 3.6 μm and then spaced vertically for clarity. The spectra are each offset relative to the second spectrum from the bottom in increments of 0.22 units. Red dashed lines superimposed on the spectra indicate third-order polynomial continuum fits. The H_2O_2 band can be seen clearly at 3.5 μm in the most poleward spectra. (**B**) Corresponding continuum-removed H_2O_2 bands for the leading-hemisphere latitude bins. Red dashed lines indicate the continuum level. Fits of Europa's leading-hemisphere H_2O_2 absorption (*21*) to the strongest Ganymede bands are shown in blue, where Europa's band has been scaled to ~69% of its strength for both the top and bottom bins. Here, we fit the Europa continuum using an identical approach to that which we take for Ganymede. The excellent match between the confirmed H_2O_2 band on Europa and Ganymede's 3.5 μm feature definitively identifies the presence of H_2O_2 on Ganymede. (**C**) Average spectra for the same 30° latitude bins on the trailing hemisphere, where the H_2O_2 feature is only weakly seen, even in the polar-most averages. The spectra are each offset relative to the third spectrum from the bottom in increments of 0.22 units. (**D**) Corresponding continuum-removed spectra for the trailing-hemisphere latitude bins. For all panels (A) to (D), the latitudinal averages contain all pixels on the disk with centers within the given latitude ranges and range from averages of ~5 pixels for the highest-latitude bins to ~68 pixels for the lowest-latitude bins.

Differences in state between the O_2 and H_2O_2 may help explain this spatial disparity. The laboratory work of (*25*) suggests that, on Europa, which spans an 80 to 130 K temperature range also relevant to the upper latitudes of Ganymede (*36*–*39*), H_2O_2 may exist in isolated trimers of $H_2O_2{\cdot}2H_2O$ dispersed in water ice. The surface O_2 of both satellites, on the other hand, must be physically trapped in some way, as condensed O_2 is highly unstable at the surface temperatures and pressures of the Galilean moons (*40*–*42*). Although it has been suggested that solid O_2 may exist within cold patches or a cold subsurface layer on Ganymede (*41*, *42*), observations that the surface O_2 exists at the warmest latitudes with no apparent correlation to albedo (*15*) makes a cold-trapping explanation unlikely. Instead, the leading suggestion is that bubbles of radiolytically produced O_2 become confined within voids in the ice (*43*), and the trapping of O_2 in irradiated water ice has been seen in the laboratory (*44*, *45*). The disruption of such bubble inclusions by charged-particle sputtering, as originally suggested in (*43*), may explain their association with the trailing-hemisphere equatorial latitudes, which are understood to receive the lowest sputtering fluxes (*13*, *19*, *46*), as well as their absence from the highly bombarded polar

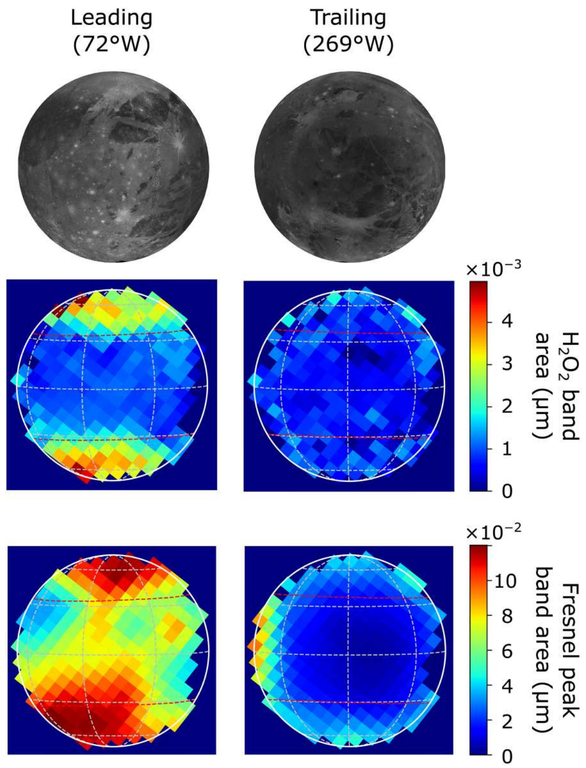

Fig. 2. Maps of Ganymede's 3.5 μm H_2O_2 absorption compared to those of the 3.1 μm Fresnel peaks of water ice and corresponding projections of the U.S. Geological Survey *Voyager-Galileo* imaging mosaic. H_2O_2 appears constrained to the upper latitudes, particularly on the leading hemisphere, which exhibits sharp boundaries at approximately ±30° to 35° latitude. These boundaries are roughly coincident with the onset of Ganymede's polar frost caps (*17*, *18*) and with the latitudes at which most of the impinging Jovian magnetospheric particles can access the surface (*13*, *18*). Maps of the Fresnel reflection peak of water ice, which generally track the distribution of ice deduced from shorter-wavelength water bands (*28*, *29*), also show the areas of greatest H_2O_2 on the leading hemisphere to be enriched in water ice. The trailing hemisphere shows comparatively weak Fresnel reflections and, overall, less-icy spectra. This hemispheric dichotomy in water ice may help explain the leading/trailing contrast in H_2O_2, while the overall polar H_2O_2 distribution may reflect a combination of precursor water availability and temperature and/or radiation intensity effects. The approximate average boundary between open and closed field lines from (*18*) are included as red dashed lines. The 60°S, 30°S, 0°N, 30°N, and 60°N parallels are also included in gray for both hemispheres. The leading-hemisphere map includes the 45°W, 90°W, and 135°W meridians, while the trailing-hemisphere map shows those for 225°W, 270°W, and 315°W. The *Voyager-Galileo* mosaic used can be found at https://astrogeology.usgs.gov/search/map/Ganymede/Voyager-Galileo/Ganymede_Voyager_GalileoSSI_global_mosaic_1km.

latitudes (*15*). Disruption of the surface trapping by dust impacts may also be an important factor, although charged dust dynamics are complex (*47*–*49*) and not entirely understood. Thus, the geography of the surface O_2 may not accurately reflect O_2 production efficiency from water-ice radiolysis, but rather entirely depend on physical factors controlling its trapping mechanism. O_3, though somewhat less volatile than O_2 (*50*), is less readily seen from the irradiation of pure H_2O ice (*51*) and seems to require efficient trapping of precursor radiolytic O_2 to form in detectable amounts (*44*, *52*). Thus, O_3 may best form within the proposed O_2 bubble inclusions, as originally posited in (*43*), thereby explaining its own trailing-hemisphere enhancement.

As H_2O_2 forms via the irradiation of pure H_2O (*53*–*56*) and does not require a physical trapping mechanism to remain stable (*25*, *54*), its geography may reasonably depend on different factors. Aside from requiring water ice and sufficient irradiation as precursors to formation, laboratory irradiation experiments also consistently find inverse relationships between the amount of produced H_2O_2 and ice temperature (*54*, *56*–*58*). These trends have been attributed to the diffusion of OH and H radicals, resulting in recombination back to H_2O and larger destruction cross sections of H_2O_2. The mobility of OH, in particular, increases markedly with temperature from ~90 to 120 K (*2*, *59*, *60*), allowing the radicals to readily diffuse from the particle tracks, hindering H_2O_2 formation and possibly disrupting already formed H_2O_2 (*54*, *56*).

Consideration of these effects predicts that, if present, H_2O_2 on Ganymede should be concentrated in the cold, icy, and irradiated polar regions and largely absent from the warmer, less-icy, and comparatively shielded equatorial latitudes, which is precisely what we observe. Although the availability of precursor ice may account for the contrast in H_2O_2 band area between the leading and trailing high latitudes, temperature and/or radiation dependence are required to explain the sharp latitudinal boundaries on the leading hemisphere. Temperature could be a natural explanation, as the equatorial regions can exceed 150 K, while the mid and upper latitudes experience cooler ~90 to 130 K temperatures for much of the day (*36*, *37*). However, the close correspondence between the detected H_2O_2 and the boundary between the open and closed field lines in Ganymede's magnetosphere (Fig. 2) suggests that increased radiolysis from the associated precipitating charged particles is important. It is possible that future spectra with higher spatial resolution, in combination with further understanding of Ganymede's geographically varying surface temperatures, may help deconvolve these effects. In addition, observations covering the leading/anti-Jovian quadrant, where potentially substantial numbers of high-energy ions may reach equatorial latitudes (*13*, *61*), might also help differentiate between irradiation and temperature dependence.

Nevertheless, Ganymede's H_2O_2 distribution appears exactly as expected based on our laboratory understanding of water-ice radiolysis, which places it in stark contrast to neighboring Europa, whose H_2O_2 appears to defy the same expectations. Rather than similarly following the coldest, iciest regions at its leading-hemisphere upper latitudes (*62*, *63*), Europa's 3.5 μm H_2O_2 bands are strongest at the comparatively warm equator (*38*, *64*, *65*), apparently associated with salty, non-ice terrain (*66*). It is also not clear how and whether Europa's H_2O_2 distribution is controlled by the local precipitation of charged particles. Although roughly coincident with the bombardment of the highest-energy (≥20 MeV) electrons (*67*, *68*), Europa's H_2O_2 does not obviously relate to the precipitation of the more abundant lower-energy electrons (*67*, *69*), which primarily affect the equatorial trailing hemisphere, or the precipitation of energetic ions, which can affect both hemispheres and are not expected to be constrained to the low latitudes (*67*, *70*, *71*). Ions have higher initial linear energy transfer (LET), which simplified extrapolation from some laboratory studies (*54*, *56*) might suggest that they would be more effective than electrons at generating H_2O_2. However, as such an extrapolation does not account for the fact that a particle's LET changes along its trajectory through the ice or other unknown potentially complicating dependencies on the particle species and energy, it may be an oversimplification with limited ability to predict the expected H_2O_2 production on Europa. Nevertheless, Europa's H_2O_2 distribution does not straightforwardly follow expectations based on temperature, ice abundance, or particle irradiation patterns.

The only similarity between the distribution observed on Ganymede and that observed on Europa is that they both exhibit far less H_2O_2 absorption on their trailing hemispheres than they do on their leading sides. On Europa, it is possible that underlying ice abundance (relative to non-ice materials) is responsible for this dichotomy (*21*, *66*), as we suggest may be the case for Ganymede. Another possibility is that SO_2 (*72*–*74*) formed as a result of the preferential sulfur bombardment of Europa's trailing hemisphere (*67*) acts to deplete H_2O_2 via thermal reactions that produce sulfate (*75*). However, while similar reactions warrant consideration for Ganymede, they may present a less viable mechanism for its trailing hemisphere, as models suggest that Ganymede's intrinsic magnetic field should direct most of the impinging sulfur ions to the high latitudes of both hemispheres (*13*, *61*).

It is not clear how the same underlying radiation processes can lead to such disparate distributions on these two icy Galilean satellites. A possible explanation suggested for Europa is that CO_2 within the non-ice terrain may act to enhance H_2O_2 yields (*66*), a phenomenon that has been seen by limited laboratory experiments investigating ice mixtures with greater relative proportions of CO_2 than those expected for the Galilean satellites (*58*, *76*). Although a possible correlation between H_2O_2 and CO_2 has been suggested from limited, low-quality *Galileo* Near Infrared Mapping Spectrometer (NIMS) data (*77*), this hypothesis has yet to be rigorously tested on Europa. The surface of Ganymede also contains CO_2, which was clearly detected by *Galileo* NIMS via its ~4.26 μm ν_3 band at low to mid latitudes of both the leading and trailing hemispheres (*27*, *78*), apparently uncorrelated with the now detected H_2O_2, and by *Juno* JIRAM, which also noted latitudinal differences (*24*). However, stability arguments and the slightly blue-shifted ν_3 band position of this CO_2, in combination with high spatial resolution observations, suggest that it is trapped or bound in a host material that is spatially segregated from water ice at the fine scale (*27*), which may make it unlikely to influence ice radiolysis and the production/destruction of H_2O_2. Furthermore, as discussed above, the low latitudes at which most of this bound CO_2 is found are substantially warmer than the equator of Europa and may simply be too warm for the production of H_2O_2. Nevertheless, it remains possible that more minor concentrations of CO_2 or of another electron scavenger may still be acting to enhance the presence of H_2O_2 at the high latitudes.

Despite lingering questions on the balance of controls in water-ice radiolysis on these satellites, the detection of H_2O_2 constrained to Ganymede's irradiated, frost-covered polar caps provides an important perspective on this process and a window into how Ganymede's own magnetic field influences the alteration of its surface chemistry. Future laboratory experiments targeting the relative influence of temperature, composition, and radiation controls on H_2O_2 yield, in addition to chemical modeling of the numerous reaction pathways possible during water-ice radiolysis, may help us arrive at a unified understanding of how these processes operate on icy bodies throughout the solar system.

MATERIALS AND METHODS

Reduction of JWST NIRSpec data

We analyze JWST NIRSpec observations of Ganymede obtained as part of the Solar System ERS program #1373 (*79*). The observations were taken using the IFU, F290LP filter, and G395H high-resolution grating, which provided a resolving power of ~2700 and a wavelength coverage of 2.9 to 5.2 μm. Details concerning the dates, geometries, and exposure times associated with each visit are given in Table 1.

As of the time of this analysis, the standard JWST pipeline (version #1.8.5) fails to appropriately combine the multiple dithered observations of Ganymede, does not correct for 1/*f* frequency-dependent noise in the detectors, and artificially induces low-to-medium frequency wave–like structures in the spectra of targets observed with the IFU. Much of this latter problem appears in the "CubeBuild" step of the analysis, where the data from individual one-dimensional slits are interpolated and combined into a two-dimensional image at every wavelength.

To circumvent these issues, we begin our data analysis with the level 2 "rate" files, which are the two-dimensional calibrated output files from the instrument. Examination of these files readily shows the effects of 1/*f* signal modulation caused by electronic drifts during the detector readout. Many of the detector pixels are not exposed to sky and so can be used to measure and remove this modulation. We use the level 2 "cal" files to find unilluminated pixels, and for each pixel in the "rate" image, we take the median of all unilluminated pixels in a column within ±150 rows to define the modulation and subtract it from the rate image. The standard level 2 pipeline is then run on these modified rate files. The final step in the standard level 2 pipeline is the CubeBuild, which converts the one-dimensional spectra to image cubes. We circumvent much of the interpolation required for this mapping by forcing the pipeline to build the cubes with one axis parallel to the slits and one perpendicular to the slits (using the "ifualign" geometry in CubeBuild). A single row of these cubes corresponds to a single slit, and the resulting image cubes have a 0.1 arc sec × 0.1 arc sec spatial pixel size.

Each Ganymede observation consists of four dithers (with only small positional changes between the dithers owing to the fact that Ganymede nearly fills the IFU), and at high spectral resolution, the spectrum is dispersed onto two separate detectors ("NRS1" and "NRS2"). Each data file from the separate detectors and different dithers is analyzed as above. To combine the dithers into a single image, we first use a cross-correlation to determine the offset from one cube to the next, and we shift the cubes to be spatially aligned. We make no attempt at subpixel shifting, thus possibly degrading the spatial resolution by as much as half of a spatial pixel, but we deem this degradation an acceptable trade for maintaining the integrity of the original data. To combine the four dithers, we apply a scaling to each of the four spectra at each spatial pixel to normalize the spectra to the same median flux level across all wavelengths, and we then take the median of the four spectra at each wavelength value to construct the final combined spectrum in each spatial pixel. Bad pixels are common in the data and are identified by the standard pipeline. If a spatial pixel has more than one bad pixel at a given wavelength, the mean of the remaining good pixels is used.

All of the detected light from Ganymede is reflected sunlight. At the high spectral resolution of these observations, understanding the detailed spectrum of the sun is critical to calibrating the reflectance from Ganymede. We use JWST observations of the G0V star P330-E (*80*) taken in an identical setting to both measure a solar analog spectrum and calibrate the spectral response of JWST. The stellar observations are reduced identically to the Ganymede observations except for the combination step, where we do simple point spread function (PSF) fitting to extract a spectrum at each dither position and then take a median of the dither positions for the final spectrum. Most of the narrow features seen in the Ganymede spectra are solar absorption features. We construct relative Ganymede reflectance spectra by dividing Ganymede by the G0V spectrum, allowing for subpixel shifts in wavelength to achieve the best possible cancelation of stellar features. The spectra are presented in the JWST observer frame, as the Doppler shift imparted by Ganymede's topo- and heliocentric velocities is negligibly small ($<4.5 \times 10^{-4}$ μm) for the evaluation of the broad features we discuss.

We then inspect the resulting spectrum associated with each spatial pixel for signs of remaining artifacts. Although our approach precludes most of the wavelength-dependent pixel-to-pixel flux errors, which manifest as low- to mid-frequency wave–like structures in the spectra, some limb spatial pixels are still unavoidably affected. For such pixels, the artificial structure appears to be entirely due to the instrument undersampling the PSF such that pipeline rectification of the slits introduces flux oscillations that are especially strong for regions of rapidly changing brightness, like Ganymede's limbs. We flag these few spatial pixels, for which the measurement of weak features may be unreliable, and exclude them from our analysis.

Last, we determine the geometry of the image cubes and the geographic coordinates of each spatial pixel on Ganymede. We define the subpixel center of Ganymede in each cube by finding the center location that maximizes the total flux included within a disk of Ganymede's angular diameter for the corresponding observation times. Then, we calculate the coordinates of each spatial pixel within the defined limb of Ganymede using the position angle information from the FITS file headers and the corresponding rotational phase and north polar angle of Ganymede. We obtain all of the aforementioned geometric information for Ganymede from JPL Horizons (https://ssd.jpl.nasa.gov/horizons/).

Measurement of band areas and estimates of concentrations

To isolate the H_2O_2 absorption in each spatial pixel of the Ganymede cubes, we remove polynomial continua from each spectrum, adjusting the bounds of the fitting region to most conservatively avoid attributing slight inconsistencies in fitting the spatially varying continuum shape to residual H_2O_2 absorption. We use third-order polynomials, as they reasonably approximate the geographically varying continuum, particularly in the absence of visible H_2O_2 bands, without introducing obviously spurious curvature. For the leading hemisphere, we fit a third-order polynomial from 3.4 to 3.65 μm, excluding the visible band from 3.45 to 3.61 μm, making very slight adjustments, if necessary, to match the background continuum. We then remove the fitted continuum and integrate the residual absorption to give the band area of the feature. For the trailing hemisphere, we find the need to more frequently adjust the ranges included in defining the fits, but always by only hundredths of a micrometer. In all cases, the residual areas are integrated from 3.44 to 3.59 μm. Given the shape of the H_2O_2 band, this range likely slightly underestimates the true band area of strong absorptions by cutting into the long-wavelength tail, but we deem this acceptable, as we also find that it allows us to consistently minimize errors in fitting the drastically changing continua for places without visible H_2O_2 absorption.

For our maps, we estimate the spatial pixel-to-pixel uncertainty associated largely with errors in consistently defining the unknown continuum to be approximately $\pm 4 \times 10^{-4}$ μm of band area. We also emphasize that very small band areas ($\leq 1.5 \times 10^{-3}$ μm) near the equator, where we see no clearly distinct H_2O_2 absorption (Fig. 1), might be at least partly attributed to general discrepancies between the true continuum shape and the assumed third-order polynomials. We take a similar approach to measuring the water-ice Fresnel reflectance peaks. We simply fit a straight line beneath the peak from 3 to 3.27 μm, including 0.03 μm on either side in the polynomial fit, divide out this fitted continuum, and integrate the residual area under the peaks as a proxy for the peak strength.

To estimate the optically sensed column densities and approximate abundances of H_2O_2 relative to water for average spectra of Ganymede's polar caps, we follow the example used for ground-based observations of Europa (*21*). For direct comparison, we use the same laboratory-derived band strength value of 5×10^{-17} cm per molecule for a temperature of 100 K, which is based on the experimental measurements of (*54*), the same ice density of 3×10^{22} molecules/cm^3, and the same assumed optical depth and grain size of 50 μm. This grain size falls within the estimated range of ice grain sizes between the onset of Ganymede's polar caps at mid latitudes and its poles (*26*). Performing the same calculation for the high-quality ground-based spectrum of Europa's leading hemisphere, we estimate values roughly a factor of 2 lower than deduced in (*21*), which we attribute to differences in the polynomial fits used. If we instead take a second-order polynomial with slightly wider bounds, which does not match the continuum of Ganymede well, we find a value for Europa that is consistent with the 1σ range of (*21*). We note that, in all cases, our estimates are quite approximate and inherently depend on the exact fitting parameters used to determine the integrated absorbance of the H_2O_2 band, the assumed temperature, and assumptions about the optical path and surface ice density.

REFERENCES AND NOTES

1. R. E. Johnson, R. W. Carlson, J. F. Cooper, C. Paranicas, M. H. Moore, M. C. Wong, Radiation effects on the surfaces of the Galilean satellites, in *Jupiter: The Planet, Satellites and Magnetosphere*, F. Bagenal, T. Dowling, W. McKinnon, Eds. (Cambridge Univ. Press, 2004), pp. 485–512.
2. R. E. Johnson, T. I. Quickenden, Photolysis and radiolysis of water ice on outer solar system bodies. *J. Geophys. Res. Planets* **102**, 10985–10996 (1997).
3. D. T. Hall, D. F. Strobel, P. D. Feldman, M. A. McGrath, H. A. Weaver, Detection of an oxygen atmosphere on Jupiter's moon Europa. *Nature* **373**, 677–679 (1995).
4. D. T. Hall, P. D. Feldman, M. A. McGrath, D. F. Strobel, The far-ultraviolet oxygen airglow of Europa and Ganymede. *Astrophys. J.* **499**, 475–481 (1998).
5. M. A. McGrath, E. Lellouch, D. F. Strobel, P. D. Feldman, R. E. Johnson, Satellite atmospheres, in *Jupiter: The Planet, Satellites and Magnetosphere*, F. Bagenal, T. Dowling, and W. McKinnon, Eds. (Cambridge Univ. Press, 2004), pp. 457–483.
6. N. J. Cunningham, J. R. Spencer, P. D. Feldman, D. F. Strobel, K. France, S. N. Osterman, Detection of Callisto's oxygen atmosphere with the Hubble Space Telescope. *Icarus* **254**, 178–189 (2015).
7. J. R. Spencer, W. M. Calvin, M. J. Person, Charge-coupled device spectra of the Galilean satellites: Molecular oxygen on Ganymede. *J. Geophys. Res.* **100**, 19049 (1995).
8. J. R. Spencer, W. M. Calvin, Condensed O_2 on Europa and Callisto. *Astron J.* **124**, 3400–3403 (2002).

9. K. S. Noll, R. E. Johnson, A. L. Lane, D. L. Domingue, H. A. Weaver, Detection of ozone on Ganymede. *Science* **273**, 341–343 (1996).
10. A. R. Hendrix, C. A. Barth, C. W. Hord, Ganymede's ozone-like absorber: Observations by the Galileo ultraviolet spectrometer. *J. Geophys. Res. Planets.* **104**, 14169–14178 (1999).
11. M. G. Kivelson, K. K. Khurana, C. T. Russell, R. J. Walker, J. Warnecke, F. v. Coroniti, C. Polanskey, D. J. Southwood, G. Schubert, Discovery of Ganymede's magnetic field by the Galileo spacecraft. *Nature* **384**, 537–541 (1996).
12. M. G. Kivelson, K. K. Khurana, F. v. Coroniti, S. Joy, C. T. Russell, R. J. Walker, J. Warnecke, L. Bennett, C. Polanskey, The magnetic field and magnetosphere of Ganymede. *Geophys. Res. Lett.* **24**, 2155–2158 (1997).
13. A. R. Poppe, S. Fatemi, K. K. Khurana, Thermal and energetic ion dynamics in Ganymede's magnetosphere. *J. Geophys. Res. Space Phys.* **123**, 4614–4637 (2018).
14. W. M. Calvin, J. R. Spencer, Latitudinal distribution of O_2 on Ganymede: Observations with the Hubble space telescope. *Icarus* **130**, 505–516 (1997).
15. S. K. Trumbo, M. E. Brown, D. Adams, The geographic distribution of dense-phase O_2 on Ganymede. *Planet. Sci. J.* **2**, (2021).
16. P. M. Molyneux, T. K. Greathouse, G. R. Gladstone, M. H. Versteeg, V. Hue, J. Kammer, M. W. Davis, S. J. Bolton, R. Giles, J. E. P. Connerney, J. C. Gérard, D. C. Grodent, Ganymede's UV reflectance from Juno-UVS data. *Geophys. Res. Lett.* **49**, e2022GL099532 (2022).
17. B. A. Smith, L. A. Soderblom, R. Beebe, J. Boyce, G. Briggs, M. Carr, S. A. Collins, A. F. Cook, G. E. Danielson, M. E. Davies, The Galilean satellites and Jupiter: Voyager 2 imaging science results. *Science* **206**, 927–950 (1979).
18. K. K. Khurana, R. T. Pappalardo, N. Murphy, T. Denk, The origin of Ganymede's polar caps. *Icarus* **191**, 193–202 (2007).
19. C. Plainaki, A. Milillo, S. Massetti, A. Mura, X. Jia, S. Orsini, V. Mangano, E. de Angelis, R. Rispoli, The H2O and O2 exospheres of Ganymede: The result of a complex interaction between the Jovian magnetospheric ions and the icy moon. *Icarus* **245**, 306–319 (2015).
20. R. W. Carlson, M. S. Anderson, R. E. Johnson, W. D. Smythe, A. R. Hendrix, C. A. Barth, L. A. Soderblom, G. B. Hansen, T. B. McCord, J. B. Dalton, Hydrogen peroxide on the surface of Europa. *Science* **283**, 2062–2064 (1999).
21. K. P. Hand, M. E. Brown, Keck II observations of hemispherical differences in H_2O_2 on Europa. *Astrophys. J. Lett.* **766**, L21 (2013).
22. A. R. Hendrix, C. A. Barth, C. W. Hord, A. L. Lane, Europa: Disk-resolved ultraviolet measurements using the Galileo Ultraviolet Spectrometer. *Icarus* **135**, 79–94 (1998).
23. A. R. Hendrix, C. A. Barth, A. I. F. Stewart, C. W. Hord, A. L. Lane, Hydrogen peroxide on the icy Galilean satellites, in *Lunar and Planetary Science Conference* (1999), p. 2043.
24. A. Mura, A. Adriani, R. Sordini, G. Sindoni, C. Plainaki, F. Tosi, G. Filacchione, S. Bolton, F. Zambon, C. J. Hansen, Infrared observations of Ganymede from the Jovian infrared auroral mapper on Juno. *J. Geophys. Res. Planets* **125**, e2020JE006508 (2020).
25. M. J. Loeffler, R. A. Baragiola, The state of hydrogen peroxide on Europa. *Geophys. Res. Lett.* **32**, L17202 (2005).
26. K. Stephan, C. A. Hibbitts, R. Jaumann, H2O-ice particle size variations across Ganymede's and Callisto's surface. *Icarus* **337**, 113440 (2020).
27. C. A. Hibbitts, R. T. Pappalardo, G. B. Hansen, T. B. McCord, Carbon dioxide on Ganymede. *J. Geophys. Res. Planets* **108**, 5036 (2003).
28. N. Ligier, C. Paranicas, J. Carter, F. Poulet, W. M. Calvin, T. A. Nordheim, C. Snodgrass, L. Ferellec, Surface composition and properties of Ganymede: Updates from ground-based observations with the near-infrared imaging spectrometer SINFONI/VLT/ESO. *Icarus* **333**, 496–515 (2019).
29. O. King, L. N. Fletcher, Global modelling of Ganymede's surface composition: Near-IR mapping from VLT/SPHERE. *J. Geophys. Res. Planets* **127**, e2022JE007323 (2022).
30. M. S. Bergren, D. Schuh, M. G. Sceats, S. A. Rice, The OH stretching region infrared spectra of low density amorphous solid water and polycrystalline ice Ih. *J. Chem. Phys.* **69**, 3477–3482 (1978).
31. R. M. E. Mastrapa, W. M. Grundy, M. S. Gudipati, Amorphous and crystalline H_2O-ice, in *The Science of Solar System Ices*, M. S. Gudipati, J. Castillo-Rogez, Eds. (Springer, 2013), pp. 371–408.
32. K. Stephan, M. Ciarniello, O. Poch, B. Schmitt, D. Haack, A. Raponi, VIS-NIR/SWIR spectral properties of H2O ice depending on particle size and surface temperature. *Minerals* **11**, 1328 (2021).
33. W. M. Calvin, R. N. Clark, R. H. Brown, J. R. Spencer, Spectra of the icy Galilean satellites from 0.2 to 5μm: A compilation, new observations, and a recent summary. *J. Geophys. Res. Planets* **100**, 19041–19048 (1995).
34. T. B. McCord, G. B. Hansen, C. A. Hibbitts, Hydrated salt minerals on Ganymede's surface: Evidence of an ocean below. *Science* **292**, 1523–1525 (2001).
35. L. Roth, N. Ivchenko, G. R. Gladstone, J. Saur, D. Grodent, B. Bonfond, P. M. Molyneux, K. D. Retherford, A sublimated water atmosphere on Ganymede detected from Hubble Space Telescope observations. *Nat. Astron.* **5**, 1043–1051 (2021).
36. J. R. Spencer, The surfaces of Europa, Ganymede, and Callisto: An investigation using voyager IRIS thermal infrared spectra (Jupiter), thesis, The University of Arizona (1987).
37. G. S. Orton, J. R. Spencer, L. D. Travis, T. Z. Martin, L. K. Tamppari, Galileo photopolarimeter-radiometer observations of Jupiter and the Galilean satellites. *Science* **274**, 389–391 (1996).
38. J. R. Spencer, L. K. Tamppari, T. Z. Martin, L. D. Travis, Temperatures on Europa from Galileo photopolarimeter-radiometer: Nighttime thermal anomalies. *Science* **284**, 1514–1516 (1999).
39. K. de Kleer, B. Butler, I. de Pater, M. A. Gurwell, A. Moullet, S. Trumbo, J. Spencer, Ganymede's surface properties from millimeter and infrared thermal emission. *Planet. Sci. J.* **2**, 5 (2021).
40. W. M. Haynes, D. R. Lide, T. J. Bruno, *CRC Handbook of Chemistry and Physics* (CRC Press, 2016).
41. R. A. Vidal, D. Bahr, R. A. Baragiola, M. Peters, Oxygen on ganymede: Laboratory studies. *Science* **276**, 1839–1842 (1997).
42. R. A. Baragiola, D. A. Bahr, Laboratory studies of the optical properties and stability of oxygen on Ganymede. *J. Geophys. Res. Planets* **103**, 25865–25872 (1998).
43. R. E. Johnson, W. A. Jesser, O_2/O_3 microatmospheres in the surface of Ganymede. *Astrophys. J.* **480**, L79–L82 (1997).
44. B. D. Teolis, M. J. Loeffler, U. Raut, M. Fama, R. A. Baragiola, Ozone synthesis on the icy satellites. *Astrophys. J.* **644**, L141–L144 (2006).
45. M. J. Loeffler, B. D. Teolis, R. A. Baragiola, A model study of the thermal evolution of astrophysical ices. *Astrophys J.* **639**, L103–L106 (2006).
46. G. Carnielli, M. Galand, F. Leblanc, R. Modolo, A. Beth, X. Jia, Simulations of ion sputtering at Ganymede. *Icarus* **351**, 113918 (2020).
47. H. Krüger, A. V. Krivov, D. P. Hamilton, E. Grün, Detection of an impact-generated dust cloud around Ganymede. *Nature* **399**, 558–560 (1999).
48. H. Krüger, A. v. Krivov, E. Grün, A dust cloud of Ganymede maintained by hypervelocity impacts of interplanetary micrometeoroids. *Planet. Space Sci.* **48**, 1457–1471 (2000).
49. K. Miljković, J. K. Hillier, N. J. Mason, J. C. Zarnecki, Models of dust around Europa and Ganymede. *Planet. Space Sci.* **70**, 20–27 (2012).
50. N. Fray, B. Schmitt, Sublimation of ices of astrophysical interest: A bibliographic review. *Planet. Space Sci.* **57**, 2053–2080 (2009).
51. D. A. Bahr, M. Famá, R. A. Vidal, R. A. Baragiola, Radiolysis of water ice in the outer solar system: Sputtering and trapping of radiation products. *J. Geophys. Res. Planets* **106**, 33285–33290 (2001).
52. B. M. Jones, R. I. Kaiser, G. Strazzulla, Uv-vis, infrared, and mass spectroscopy of electron irradiated frozen oxygen and carbon dioxide mixtures with water. *Astrophys. J.* **781**, 85 (2014).
53. O. Gomis, G. Leto, G. Strazzulla, Hydrogen peroxide production by ion irradiation of thin water ice films. *Astron. Astrophys.* **420**, 405–410 (2004).
54. M. J. Loeffler, U. Raut, R. A. Vidal, R. A. Baragiola, R. W. Carlson, Synthesis of hydrogen peroxide in water ice by ion irradiation. *Icarus* **180**, 265–273 (2006).
55. W. Zheng, D. Jewitt, R. I. Kaiser, Formation of hydrogen, oxygen, and hydrogen peroxide in electron-irradiated crystalline water ice. *Astrophys. J.* **639**, 534–548 (2006).
56. K. P. Hand, R. W. Carlson, H2O2 production by high-energy electrons on icy satellites as a function of surface temperature and electron flux. *Icarus* **215**, 226–233 (2011).
57. W. Zheng, D. Jewitt, R. I. Kaiser, Temperature dependence of the formation of hydrogen, oxygen, and hydrogen peroxide in electron-irradiated crystalline water ice. *Astrophys. J.* **648**, 753–761 (2006).
58. M. H. Moore, R. L. Hudson, IR detection of H_2O_2 at 80 K in ion-irradiated laboratory ices relevant to Europa. *Icarus* **145**, 282–288 (2000).
59. S. Siegel, L. H. Baum, S. Skolnik, J. M. Flournoy, Observations of the thermal behavior of radicals in γ-irradiated ice. *J. Chem. Phys.* **32**, 1249–1256 (1960).
60. A. PŁonka, E. Szajdzińska-Piętek, J. Kroh, Decay kinetics of hydroxyl radicals in frozen aqueous systems. *Radiat. Phys. Chem.* **23**, 583–587 (1984).
61. C. Plainaki, S. Massetti, X. Jia, A. Mura, A. Milillo, D. Grassi, G. Sindoni, E. D'Aversa, G. Filacchione, Kinetic simulations of the Jovian energetic ion circulation around Ganymede. *Astrophys. J.* **900**, 74 (2020).
62. M. E. Brown, K. P. Hand, Salts and radiation products on the surface of Europa. *Astron. J.* **145**, 110 (2013).
63. N. Ligier, F. Poulet, J. Carter, R. Brunetto, F. Gourgeot, VLT/SINFONI observations of Europa: New insights into the surface composition. *Astron J.* **151**, 163 (2016).
64. J. A. Rathbun, N. J. Rodriguez, J. R. Spencer, Galileo PPR observations of Europa: Hotspot detection limits and surface thermal properties. *Icarus* **210**, 763–769 (2010).
65. S. K. Trumbo, M. E. Brown, B. J. Butler, ALMA thermal observations of Europa. *Astron J.* **156**, 161 (2018).

66. S. K. Trumbo, M. E. Brown, K. P. Hand, H_2O_2 within chaos terrain on Europa's leading hemisphere. *Astron J.* **158**, 127 (2019).
67. C. Paranicas, J. F. Cooper, H. B. Garrett, R. E. Johnson, S. J. Sturner, Europa's radiation environment and its effects on the surface, in *Europa* (University of Arizona Press Tucson, 2009), pp. 529–544.
68. T. A. Nordheim, K. P. Hand, C. Paranicas, Preservation of potential biosignatures in the shallow subsurface of Europa. *Nat. Astron.* **2**, 673–679 (2018).
69. C. Paranicas, R. W. Carlson, R. E. Johnson, Electron bombardment of Europa. *Geophys. Res. Lett.* **28**, 673–676 (2001).
70. C. Paranicas, J. M. Ratliff, B. H. Mauk, C. Cohen, R. E. Johnson, The ion environment near Europa and its role in surface energetics. *Geophys. Res. Lett.* **29**, 11–18 (2002).
71. J. B. Dalton III, T. Cassidy, C. Paranicas, J. H. Shirley, L. M. Prockter, L. W. Kamp, Exogenic controls on sulfuric acid hydrate production at the surface of Europa. *Planet. Space Sci.* **77**, 45–63 (2013).
72. K. S. Noll, H. A. Weaver, A. M. Gonnella, The albedo spectrum of Europa from 2200 Å to 3300 Å. *J. Geophys. Res. Planets* **100**, 19057–19059 (1995).
73. A. L. Lane, R. M. Nelson, D. L. Matson, Evidence for sulphur implantation in Europa's UV absorption band. *Nature* **292**, 38–39 (1981).
74. T. M. Becker, S. K. Trumbo, P. M. Molyneux, K. D. Retherford, A. R. Hendrix, L. Roth, U. Raut, J. Alday, M. A. McGrath, Mid-ultraviolet hubble observations of Europa and the global surface distribution of SO_2. *Planet. Sci. J.* **3**, 129 (2022).
75. M. J. Loeffler, R. L. Hudson, Low-temperature thermal reactions between SO_2 and H_2O_2 and their relevance to the jovian icy satellites. *Icarus* **224**, 257–259 (2013).
76. G. Strazzulla, G. Leto, F. Spinella, O. Gomis, Production of oxidants by ion irradiation of water/carbon dioxide frozen mixtures. *Astrobiology* **5**, 612–621 (2005).
77. R. W. Carlson, Spatial distribution of carbon dioxide, hydrogen peroxide, and sulfuric acid on Europa, in *American Astronomical Society/Division for Planetary Sciences Meeting Abstracts #33* (Bulletin of the American Astronomical Society, 2001), vol. 33, pp. 42–47.
78. T. B. McCord, R. W. Carlson, W. D. Smythe, G. B. Hansen, R. N. Clark, C. A. Hibbitts, F. P. Fanale, J. C. Granahan, M. Segura, D. L. Matson, T. V. Johnson, P. D. Martin, Organics and other molecules in the surfaces of Callisto and Ganymede. *Science* **278**, 271–275 (1997).
79. I. de Pater, T. Fouchet, M. Wong, P. Fry, L. Fletcher, R. Hueso, H. Melin, M. Showalter, D. Bockelée-Morvan, E. Lellouch, K. de Kleer, A. Conrad, L. Sromovsky, P. Rodriguez-Ovalle, P. Irwin, J. Stansberry, B. Holler, JWST-ERS 1373 Team, A. Glasse, D. Law, A. Noriega-Crespo, M. Garcia Marin, JWST observations of the Jovian system from commissioning and ERS data, in AAS Division of Planetary Sciences Meeting #54 (Bulletin of the American Astronomical Society, 2022), p. 306.07.
80. K. D. Gordon, R. Bohlin, G. C. Sloan, G. Rieke, K. Volk, M. Boyer, J. Muzerolle, E. Schlawin, S. E. Deustua, D. C. Hines, The James Webb Space Telescope absolute flux calibration. I. Program design and calibrator stars. *Astron. J.* **163**, 267 (2022).

Acknowledgments: This work is based on observations made with the NASA/ESA/CSA James Webb Space Telescope. The data were obtained from the Mikulski Archive for Space Telescopes at the Space Telescope Science Institute, which is operated by the Association of Universities for Research in Astronomy Inc., under NASA contract NAS 5-03127 for JWST. These observations are associated with program #1373, which is led by co-PIs (principal investigators) Imke de Pater and Thierry Fouchet and has a zero-exclusive-access period. **Funding:** S.K.T. was supported by a Heising-Simons Foundation *51 Pegasi b* postdoctoral fellowship (2021-2663). L.N.F. was supported by a European Research Council Consolidator Grant (under the European Union's Horizon 2020 research and innovation programme, grant agreement no. 723890) at the University of Leicester. I.d.P. and M.H.W. were in part supported by the Space Telescope Science Institute grant no. JWST-ERS-01373. **Author contributions:** S.K.T. performed the analysis, led the interpretation, and wrote the manuscript. M.E.B. reduced the JWST data and aided in interpretation and manuscript writing. I.d.P. and T.F. are the co-PIs of the Director's Discretionary Early Release Science (DD-ERS) proposal on the Jovian system that obtained the data. M.H.W., D.B.-M., L.N.F., K.d.K., E.L., O.P., M.R.S., and M.S.T. all contributed substantially to the planning and definition of the resulting observations. P.R.-O. contributed to the reduction of the Ganymede JWST observations. E.Q., F.T., S.C., and A.M. contributed helpful comments, interpretations, and expertise during manuscript preparation. **Competing interests:** The authors declare that they have no competing interests. **Data and materials availability:** The data used in this work are available at the NASA Mikulski Archive for Space Telescopes (https://archive.stsci.edu/) under program #1373. All data needed to evaluate the conclusions in the paper are present in the paper and/or the Supplementary Materials.

Submitted 20 December 2022
Accepted 21 June 2023
Published 21 July 2023
10.1126/sciadv.adg3724